**CHEMISTRY OF MATERIALS**

Article

# (M,Ru)O$_2$ (M = Mg, Zn, Cu, Ni, Co) Rutiles and Their Use as Oxygen Evolution Electrocatalysts in Membrane Electrode Assemblies under Acidic Conditions

David L. Burnett, Enrico Petrucco, Katie M. Rigg, Christopher M. Zalitis, Jamie G. Lok, Reza J. Kashtiban, Martin R. Lees, Jonathan D. B. Sharman, and Richard I. Walton*

Read Online

ACCESS | Metrics & More | Article Recommendations | SI Supporting Information

**ABSTRACT:** The rutiles (M,Ru)O$_2$ (M = Mg, Zn, Co, Ni, Cu) are formed directly under hydrothermal conditions at 240 °C from potassium perruthenate and either peroxides of zinc or magnesium or poorly crystalline oxides of cobalt, nickel, or copper. The polycrystalline powders consist of lath-shaped crystallites, tens of nanometres in maximum dimension. Powder neutron diffraction shows that the materials have an expanded $a$ axis and contracted $c$ axis compared to the parent RuO$_2$, but there is no evidence of lowering of symmetry to other AO$_2$-type structures, supported by Raman spectroscopy. Rietveld refinement shows no evidence for oxide non-stoichiometry and provides a formula (M$_x$Ru$_{1-x}$)O$_2$ with 0.14 < $x$ < 0.2, depending on the substituent metal. This is supported by energy-dispersive X-ray analysis on the transmission electron microscope, while Ru K-edge XANES spectroscopy shows that upon inclusion of the substituent the average Ru oxidation state is increased to balance charge. Variable temperature magnetic measurements provide evidence for atomic homogeneity of the mixed metal materials, with suppression of the high temperature antiferromagnetism of RuO$_2$ and increased magnetic moment. The new rutiles all show enhanced electrocatalysis compared to reference RuO$_2$ materials for oxygen evolution in 1 M H$_2$SO$_4$ electrolyte at 60 °C, with higher specific and mass activity (per Ru) than a low surface area crystalline RuO$_2$ and with less Ru dissolution over 1000 cycles compared to an RuO$_2$ with a similar surface area. Magnesium substitution provides the optimum balance between stability and activity, despite leaching of the Mg$^{2+}$ into solution, and this was proved in membrane electrode assemblies.
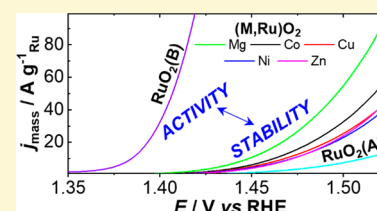
## INTRODUCTION

Ruthenium dioxide adopts the rutile structure and is a material that has been well-studied because of various functional properties, including its magnetism,[1] use in electrocatalysis,[2] and as a host for lithium insertion.[3] These important areas have each seen a resurgence of interest in the past few years due to both practical applications and fundamental understanding of the properties of the solid state. In terms of magnetic properties, study of oxides of 4d and 5d metals has attracted attention due to exotic phenomena in the solid state associated with highly correlated electrons due to greater covalency and spin−orbit coupling compared to 3d analogues.[4] RuO$_2$ itself has been part of this focus, and Berlijn et al. recently reported new experimental data that demonstrated how antiferromagnetic order persists up to at least 300 K, despite the long-held view of the material as a Pauli paramagnet.[5] In electrocatalysis, RuO$_2$ is one of the most active materials to catalyze the oxygen evolution reaction (OER) from water under acid conditions,[6−8] which is of contemporary interest in energy devices, such as proton exchange membrane electrolyzers,[9,10] while intercalation of lithium into RuO$_2$ has seen renewed interest as an anode for rechargeable batteries.[11−13]

Of relevance to tuning the properties of RuO$_2$ for practical applications, it is useful to consider the partial substitution of ruthenium by a second element. As well as diluting the amount of precious metal, which may be important from a commercial point of view, this may confer stability on the material; for example, in acid electrolytes, it is well-known that a solid solution with IrO$_2$ improves corrosion resistance,[14−16] while TiO$_2$−RuO$_2$ or SnO$_2$−RuO$_2$ solid solutions provide robust and stable electrodes.[17,18] In some cases, the electrocatalytic behavior can be tailored for application by such alloying of oxides; for example, Sn substitution in RuO$_2$ has been claimed to improve the selectivity for electrocatalytic chlorine production.[19] Recently, Cr$^{4+}$-containing RuO$_2$ has been shown to be an active and robust electrocatalyst for OER.[20] A range of lightly substituted RuO$_2$ materials including divalent substituents, such as Zn,[21,22] Ni,[23] Mg,[24] and Co,[25] have been reported with compositions (M$_{1-x}$Ru$_x$)O$_2$ and $x$ up to ∼0.3. Although these are actually considered to be intergrowths rather than homogeneous solid solutions, some show tunable properties to enhance electrocatalytic behavior.[21] Aliovalent substitution would be expected
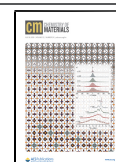
to shift the oxidation state of ruthenium away from 4+, assuming oxygen stoichiometry is maintained, leading to a change of the d-electron count and thus altering the magnetic and electronic properties; this could also be of relevance to tuning properties for applications.

The reported synthetic routes to substituted $RuO_2$ materials typically use a sol–gel-type approach, involving a precipitation of an amorphous mixed oxide followed by heat treatment at 400 °C to induce crystallinity.[21−25] Herein, we describe a hydrothermal synthesis method to substituted $RuO_2$ materials, with the aim of developing a solution-mediated crystallization that may allow atomically homogeneous materials to be produced and with potential for the formation of unusual crystal morphologies. The starting point for our synthetic approach was the use of potassium perruthenate, $KRuO_4$, as an oxidizing reagent, which has been used by us[26−29] and others[30,31] as a precursor for the hydrothermal crystallization of a number of new ternary oxides that include ruthenium. This includes antiferromagnetic $SrRu_2O_6$ with an unusually high Néel temperature,[27] a new polymorph of $Ag_3RuO_4$ with a unprecedented cation-order NiAs-type structure,[30] and the hexagonal perovskite $Ba_4Ru_3O_{10.2}(OH)_{1.8}$ that adopts an unusual structural stacking sequence.[28] In these examples, reaction between $KRuO_4$ and either a peroxide or an oxide is brought about simply by heating in water at around 240 °C, providing a convenient way to access highly crystalline oxides of ruthenium, avoiding reduction to ruthenium metal, which may easily occur on heating at elevated temperatures even in air. We report an exploration of this method as a route to other ternary ruthenium oxides and describe a set of rutile-type oxides $(Ru_{1−x}M_x)O_2$ (M = Mg, Zn, Cu, Ni, Co). We have characterized the materials using various analytical techniques and have measured their electrocatalytic properties, including use in membrane electrode assemblies to assess their potential for use in devices such as electrolyzers for water splitting.

## ■ EXPERIMENTAL SECTION

**Synthesis.** Substituted rutile materials were synthesized using potassium perruthenate (Alfa Aesar, 98%) and metal (M) peroxide or oxide (see below) in a molar ratio Ru:M of 1:0.5 in 10 mL of $H_2O$, respectively, based on 2.45 mmol of Ru. The mixtures were sealed in 23 mL Teflon-lined steel autoclaves and heated to 240 °C for 24 h in a preheated fan oven. The black powders were then collected via vacuum filtration and stirred in 50 mL of 3 M nitric(V) acid, to remove any hydroxide or oxide byproducts. The duration of the acid washing was dependent on the substituent metal: the magnesium-substituted material only required 5 min, the zinc-substituted material 2 h, and the copper, cobalt, and nickel materials needed 24 h. The materials were then collected via vacuum filtration and washed with deionized water and then acetone before drying in air at 70 °C.

The precursors for the divalent substituents were poorly crystalline metal peroxides or oxides. Zinc peroxide, $ZnO_2$, was prepared from $Zn(NO_3)_2 \cdot 6H_2O$ (4.0 g), which was added to a 250 mL polypropylene bottle. The minimal volume of ammonium hydroxide 35% was added under constant stirring, and upon complete dissolution, 10 mL of hydrogen peroxide 30% was added until the solution turned white and opaque. The bottle was then sealed and heated at 100 °C for 24 h. The resulting white solid was retrieved via vacuum filtration and washed with water before being dried at 70 °C in air for 24 h. Magnesium peroxide, $MgO_2$, was prepared by a similar method, where $Mg(NO_3)_2 \cdot 6H_2O$ (3.45 g) was added to a 100 mL conical flask followed by the minimal volume of ammonium hydroxide 35% under constant stirring. Upon dissolution, hydrogen peroxide 30% (10 mL) was added until the solution turned white and opaque. The flask was then stored at 5 °C for 72 h before the resulting white solid was retrieved via centrifugation and dried at 70 °C in air for 24 h. Nickel peroxide was purchased from Sigma-Aldrich and used as received. The synthesis of peroxides of
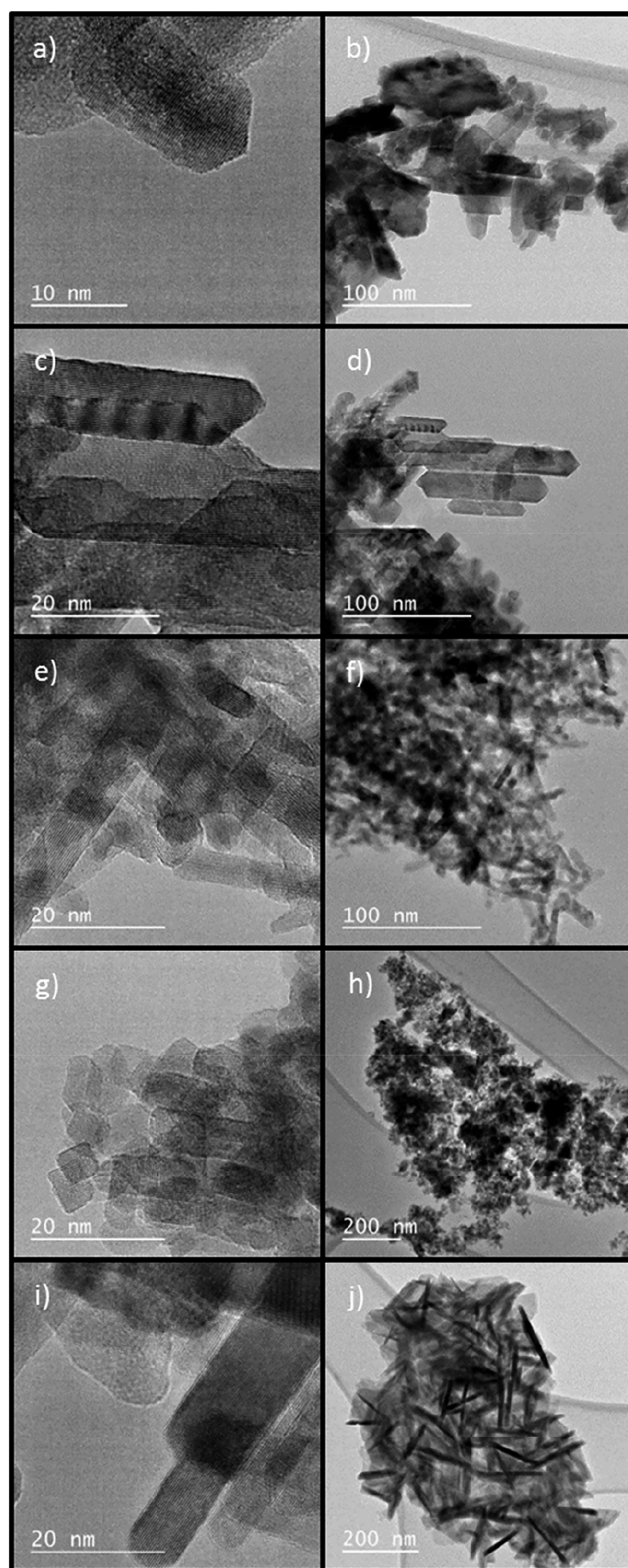


**Figure 1.** TEM images of (a and b) zinc-, (c and d) magnesium-, (e and f) nickel-, (g and h) cobalt-, and (i and j) copper-substituted ruthenium oxides each presented at two different magnifications.

copper and of cobalt was attempted by adapting the procedure of Pankratov et al.[32] Either $Cu(NO_3)_2 \cdot 2.5H_2O$ (2.0 g) or $Co(NO_3)_2 \cdot 2.5H_2O$ (2.0 g) was added to a 250 mL conical flask. To this, the minimum volume of methanol was added under constant stirring to effect complete dissolution, followed by addition of solid potassium hydroxide to the mixture, to make an approximately 1 M KOH

**Table 1. EDXA Results for Substituted Ruthenium Oxide Materials $(M,Ru)O_2$ Compared to the Composition Determined Using Structure Refinement against Powder Neutron Diffraction Data[a]**

| M | EDXA atomic M % | composition from Rietveld analysis |
|---|---|---|
| Zn | 17.4 | $Zn_{0.19}Ru_{0.81}O_2$ |
| Mg | 18.2 | $Mg_{0.17}Ru_{0.83}O_2$ |
| Ni | 16.3 | $Ni_{0.14}Ru_{0.86}O_2$ |
| Co | 14.8 | $Co_{0.15}Ru_{0.85}O_2$ |
| Cu | 13.2 | $Cu_{0.17}Ru_{0.83}O_2$ |

[a]Atomic % is given as the percentage of total metal present, with an estimated error of $\pm 2$%. The errors on refined chemical composition are given in Table 2 with the site occupancy values.

solution. To this, hydrogen peroxide 30% was added until the solution had turned completely brown. The flask was stored at 5 °C for 72 h, and the resulting brown solid was retrieved via centrifugation. The recovered materials were washed in 50 mL of distilled water for 24 h to remove excess potassium nitrate before a final vacuum filtration. The solids were dried in an oven at 70 °C for 24 h. Powder X-ray diffraction of the zinc and magnesium peroxides revealed phase-pure materials adopting cubic structures with lattice parameters close to those reported in the literature (Supporting Information). The magnesium material showed considerable peak broadening, suggesting very small crystallite size. In the case of the cobalt, nickel, and copper materials, there is no evidence that these are peroxides: powder X-ray diffraction shows the samples are poorly crystalline oxides (Supporting Information). Nevertheless, they proved to be reactive precursors for hydrothermal reaction with $KRuO_4$.

One of the ruthenium oxides used for comparison with the new substituted materials was supplied by Johnson Matthey: this was produced through the hydrolysis of ruthenium trichloride, and the hydrolysis product was then fired at 300 °C to give a highly crystalline specimen of rutile-type $RuO_2$, labeled $RuO_2(A)$. A second sample, labeled $RuO_2(B)$, was prepared as a comparison for the electrochemical studies: this was synthesized using hydrothermal reaction between $KRuO_4$ and $RuCl_3$, in the molar ratio 1:3, and heated in 1 M $H_2SO_4$ water at 240 °C for 24 h before being filtered and dried in air at 70 °C. (See the Supporting Information for characterization data.)

**Laboratory Characterization.** Samples were initially screened using powder X-ray diffraction (XRD) measured using a Siemens D5000 diffractometer (Cu $K\alpha_{1/2}$ radiation). Nonambient powder XRD measurements were made using a Bruker D8 Advance diffractometer equipped with Cu $K\alpha_{1/2}$ radiation and a VÅNTEC-1 high-speed detector. Powders were heated *in situ* using an Anton Paar XRK 900 reaction chamber controlled through a TCU 750 temperature unit. Transmission electron microscopy (TEM) was performed using a JEOL 2000FX with energy-dispersive X-ray analysis (EDXA) using an EDAX Genesis analytical system. Raman spectra were recorded on a Renishaw inVia Reflex Raman Microscope employing a 633 nm HeNe laser fitted with a Leica N Plan 50×/0.75 BD objective, and the measurements were carried out in a back scattering geometry. 0.5% of rated power was used to minimize thermal effects. Magnetization data for each material were recorded using a Quantum Design MPMS-5S SQUID magnetometer over a temperature range of 2−300 K. Zero-field-cooled warming (ZFCW) and field-cooled cooling (FCC) data were collected while a magnetic field of 1000 Oe was applied. Thermogravimetric analysis (TGA) was performed using a Mettler Toledo TGA/DSC 1 instrument under a constant flow of air (50 mL min$^{-1}$). Differential scanning calorimetry (DSC) curves were also recorded. Data were recorded from room temperature to 1000 °C at a rate of 10 °C/min. Surface area measurements were carried out using a Micrometrics Tristar 3000 porosimeter with samples degassed under nitrogen at 200 °C for 12 h. Surface areas were calculated from the adsorption isotherms using the Brunauer, Emmett, and Teller (BET) theory.

**Neutron Diffraction.** Time-of-flight powder neutron diffraction experiments were carried out on the GEM instrument, at ISIS, U.K.,[33] with powdered samples held in 6 mm diameter cylindrical cans made
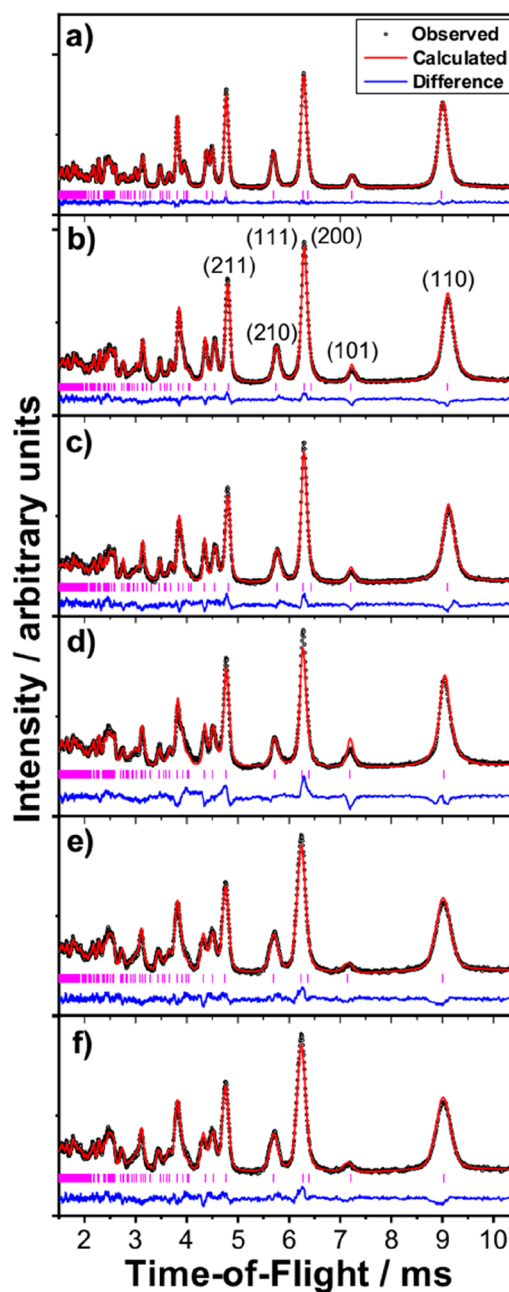


**Figure 2.** Rietveld fits to time-of-flight powder neutron diffraction data (GEM Bank 3) for (a) $RuO_2(A)$ and (b) zinc-, (c) magnesium-, (d) nickel-, (e) cobalt-, and (f) copper-substituted ruthenium oxides. The intensity scale is in arbitrary units. The Miller indices of the five largest $d$-spacing reflections are labeled in part b.

of vanadium. Structure refinement from powder diffraction data was performed using the GSAS suite of software.[34] The diffraction profile was fitted using a pseudo-Voigt peak shape (Profile Function 2 within GSAS). In the initial steps of analysis, site occupancies were set to match the metal ratios obtained by EDXA and $U_{iso}$ values were varied to reach a satisfactory fit. The site occupancies were then allowed to vary along with the $U_{iso}$ values in a refinement cycle, which resulted in only a small deviation from their initial values, with physically meaningful parameters, to give the final fits that are reported below.

**X-ray Absorption Spectroscopy.** Ru, Ni, Co, and Cu K-edge X-ray absorption near-edge structure (XANES) spectra were collected on beamline B18, at the Diamond Light Source, U.K.[35] Samples were diluted with polyethylene powder and pressed into pellets approximately 1 mm thick to optimize absorption measurements. Data were

**Table 2. Structural Details of Rutiles Obtained from Rietveld Fits to Powder Neutron Diffraction Data, for $RuO_2$ ($RuO_2$ (A)) and $(M,Ru)O_2$ Materials Using Space Group $P4_2/mnm$**

| atom | site | x | y | z | occ. | $U_{iso}/\text{Å}^2$ |
|------|------|---|---|---|------|------|
| | | | **$RuO_2$:** $a = 4.49280(4)$ Å/$c = 3.10337(4)$ Å/$V = 62.643(6)$ Å$^3$ | | | |
| Ru | 2a | 0 | 0 | 0 | 0.999(1) | 0.0107(8) |
| O | 4f | 0.30490(12) | 0.30490(12) | 0 | 1.002(2) | 0.0505(9) |
| | | | **$Zn-RuO_2$:** $a = 4.5461(2)$ Å/$c = 3.0848(2)$ Å/$V = 63.755(7)$ Å$^3$ | | | |
| Zn | 2a | 0 | 0 | 0 | 0.187(11) | 0.00137(11) |
| Ru | 2a | 0 | 0 | 0 | 0.813(11) | 0.00137(11) |
| O | 4f | 0.3031(2) | 0.3031(2) | 0 | 1.002(2) | 0.00481(10) |
| | | | **$Mg-RuO_2$:** $a = 4.5417(3)$ Å/$c = 3.0802(3)$Å/$V = 63.537(12)$ Å$^3$ | | | |
| Mg | 2a | 0 | 0 | 0 | 0.171(11) | 0.00348(17) |
| Ru | 2a | 0 | 0 | 0 | 0.829(11) | 0.00348(17) |
| O | 4f | 0.30299(19) | 0.30299(19) | 0 | 1.004(2) | 0.00320(11) |
| | | | **$Ni-RuO_2$:** $a = 4.5251(3)$ Å/$c = 3.0821$ (4) Å/$V = 63.111(13)$ Å$^3$ | | | |
| Ni | 2a | 0 | 0 | 0 | 0.141(6) | 0.00161(15) |
| Ru | 2a | 0 | 0 | 0 | 0.859(6) | 0.00161(15) |
| O | 4f | 0.3031(3) | 0.3031(3) | 0 | 1.000(2) | 0.00535(19) |
| | | | **$Co-RuO_2$:** $a = 4.5057(3)$ Å/$c = 3.0565(3)$ Å/$V = 62.063(12)$ Å$^3$ | | | |
| Co | 2a | 0 | 0 | 0 | 0.153(2) | 0.00191(15) |
| Ru | 2a | 0 | 0 | 0 | 0.847(2) | 0.00191(15) |
| O | 4f | 0.30251(17) | 0.30251(17) | 0 | 1.000(2) | 0.00270(10) |
| | | | **$Cu-RuO_2$:** $a = 4.5132(2)$ Å/$c = 3.0901(2)$ Å/$V = 62.918(7)$ Å$^3$ | | | |
| Cu | 2a | 0 | 0 | 0 | 0.173(2) | 0.00965(19) |
| Ru | 2a | 0 | 0 | 0 | 0.827(2) | 0.00965(19) |
| O | 4f | 0.30247(16) | 0.30247(16) | 0 | 1.000(2) | 0.00404(11) |

collected in transmission mode with incident energies selected using either a Si(311) (Ru K-edge) of Si(111) (for Ni, Co, and Cu K-edges) monochromator. XANES spectra were normalized to the edge step using the software ATHENA.[36] The edge position was defined as the energy at which normalized absorption equaled 0.5 in order to determine the average oxidation state.

**Membrane Electrode Assemblies.** To fabricate membrane electrode assemblies (MEAs), 0.1 g of oxide catalyst was added to 0.5 g of Hispec 1860, a commercial platinum-on-carbon catalyst. Aqueous Nafion solution (11.92 wt % solids, 1 mL) was added to produce an ink containing 110 wt % Nafion with respect to oxide catalyst. The ink was then shear-mixed in a planetary mixer using 5 mm diameter yttrium stabilized zirconia beads for 3 min at 3000 rpm. The ink was manually stirred to break apart any sediment at which point it was mixed for a further 5 min in the planetary mixer. This ink was also used for wet cell testing. The ink was screen printed onto a PTFE sheet to give a layer with an overall platinum group metal loading between 0.05 and 0.15 mg cm$^{-2}$, verified using X-ray fluorescence measurements. The layer was then transferred from the PTFE sheet onto Nafion N117, using a hot press. A Pt/C layer was simultaneously transferred to the opposite side of the Nafion N117 membrane, to produce the catalyst coated membrane. For testing, the catalyst coated membrane was placed between two flow field plates backed with microporous layer coated carbon paper, Toray TGP-H-060. Testing was carried out at 80 °C with 10 psig of humidified $H_2/N_2$ gas. The electrochemical surface areas of the platinum in both sides of the catalyst coated membrane were measured with CO stripping voltammetry. Cyclic voltammograms (CVs) were collected, scanning the potential from 0.02 to 1.6 V vs reversible hydrogen electrode at 5 mV s$^{-1}$. The membrane electrode assembly was then aged by cycling between 0.05 and 1.0 V 500 times at 100 mV s$^{-1}$. After aging, a final cyclic voltammogram was collected, scanning the potential from 0.02 to 1.6 V at 5 mV s$^{-1}$.

**Liquid Cell Electrochemistry.** For liquid cell electrochemical testing, inks were spray coated onto a Toray paper (hydrophobic gas diffusion layer 60) at 0.2 mg cm$^{-2}$ loading, verified using X-ray fluorescence (XRF) measurements. The buttons were then soaked overnight in an equivalent solution as the test solution (1 M $H_2SO_4$ (VWR AVS TITRINORM)) under a vacuum to allow ingress of solution into the gas diffusion layer, ensuring all of the catalyst is in contact with electrolyte.

A button was then placed in an electrochemical cell that contained 1 M $H_2SO_4$ while being purged with nitrogen (liquid nitrogen off gas) and held at 60 °C. A reversible hydrogen electrode (RHE) (hydrogen bubbled over Pt/C catalyst) and Pt wire was used as a reference and counter electrode, respectively. First, the cell was cycled between 0 and 1.35 V vs RHE at different scan rates (5−300 mV s$^{-1}$), and then, an activity sweep was performed between 1 and 1.55 V vs RHE at 1 mV s$^{-1}$. Then, a degradation cycle between 0.6 and 1.35 V vs RHE at 100 mV s$^{-1}$ for 1000 cycles was performed (∼4 h 10 min). This was chosen as the potential is brought up to the onset of OER, while not forming bubbles, which could affect the results. An end of life activity test was then performed after the degradation cycles equivalent to the start of life (CVs at different scan rates and then an activity sweep). The activity data were $iR$ corrected by taking the high frequency intercept of an impedance scan measured at 1.45 V vs RHE; typical values were between 0.2 and 0.35 Ω. Activity data were normalized to a mass activity by measuring the loading of the ruthenium by XRF and then assuming the ratio of the EDXA results. Degradation was monitored by taking a 1 mL sample of the electrolyte solution at the start of testing and then after the beginning of life (BOL) activity test, degradation test, and end of life (EOL) activity test for inductively coupled plasma mass spectrometry (ICP-MS) analysis. The 1 mL sample was diluted with water to 1 v.% $H_2SO_4$, and then, 1 v.% HCl was added. These samples were injected directly into an ICP-MS (Agilent Technologies 7700 series) to obtain the concentration of metal leached into solution.

## RESULTS AND DISCUSSION

Figure 1 shows electron microscopy images of the five $(M,Ru)O_2$ materials, where it can be seen that all of the substituted rutiles form lath-shaped crystallites of varying aspect ratio depending on composition. Elemental analysis using EDXA on the transmission electron microscope, Table 1, shows that for all materials the substituent metal content represents a maximum replacement of 20% of the Ru and is typically closer to 15% for most of the materials. Note that an excess of the divalent metal precursor was used in the synthesis and hydroxide byproduct removed by acid washing so the samples we have studied represent the highest substitution level by this synthesis method. The maximum

level of substitution may be governed by the ionic radius of the substituent, which is similar for all of the cations used in their divalent state and only smaller for trivalent Co. It may also be possible that the maximum oxidation state for Ru achieved under these conditions is only slightly higher than +4. The oxidation states of the metals will be discussed below.

Powder neutron diffraction was used to refine the composition and crystal structure of the substituted rutile materials by the Rietveld method, Figure 2. All powder patterns can be indexed to a tetragonal rutile phase with space group $P4_2/mnm$. The substituted materials all have an expanded $a$ axis and a contracted $c$ axis, when compared to $RuO_2$, Table 2, which is evidence of the inclusion of a substituent cation. However, there is no evidence for any significant structural distortion of the materials: the $x$ (=$y$) coordinate of the oxygen atom is rather similar for all compositions and the $c/a$ ratio, a measure of the degree of tetragonality, also changes little between the materials, much less so when compared to the range of rutile-structured dioxides reported in the literature.[37] The refined occupancies of the oxygen site are all very close to 100%, with no evidence of any non-stoichiometry. The elemental compositions deduced from the refined site occupancies of all the materials agree well with the ratios from EDXA, bearing mind the larger errors associated with the latter method, Table 1.

The mechanism of charge balance in the substituted materials is confirmed via XANES spectroscopy at the Ru K-edge, Ni K-edge, Co K-edge, and Cu K-edge, Figures 3 and 4. For all materials, Ru K-edge XANES spectroscopy shows an average ruthenium oxidation state greater than +4, close to 4.25, consistent with the occupancies extracted from the neutron diffraction. Nickel, cobalt, and copper K-edge XANES spectra, Figure 4, show that nickel and copper are found in the +2 state, while the cobalt is found in the +3 oxidation state.

The fully occupied oxygen site for all of the materials, deduced from the neutron diffraction analysis, implies that to accommodate the divalent metal a fraction of the ruthenium must be oxidized above 4+. The presence of $Co^{3+}$ in the cobalt-substituted material explains why the ruthenium in that material has a lower average ruthenium oxidation state than the other substituted materials. Thus, the composition of the new materials containing $M^{2+}$ can be written as close to $M_{0.15}^{2+}Ru_{0.55}^{4+}Ru_{0.30}^{5+}O_2$, suggesting an analogy to the mixed-metal rutile $Zn_{0.15}Ti_{0.55}Nb_{0.3}O_2$ of Abrahams et al. that contains $Ti^{4+}$ and $Nb^{5+}$ in the proportion needed to balance the charge of the lower valence third metal.[38]

Raman spectroscopy was used to confirm the local symmetry of the materials, Figure 5. The spectra show the expected $E_g$ and $A_{1g}$ bands at ~510 and 625 $cm^{-1}$, respectively, along with a less intense $B_{2g}$ band at 716 $cm^{-1}$.[39] An orthorhombic distortion can occur to the tetragonal rutile structure of $RuO_2$ when pressure is applied;[40] thus, to determine the possibility of the unit cell of the substituted materials becoming distorted due to chemical pressure, the Raman bands were fitted and full width at half-maximum (fwhm) values determined, Table 3. The ratio of the fwhm value of the $E_g$ and $A_{1g}$ modes should reveal whether any splitting in the $E_g$ band has taken place, characteristic of the orthorhombic distortion. While some variation in the $E_g/A_{1g}$ fwhm ratios is observed, there is no positive correlation with composition, and there is only a noticeable broadening of the $E_g$ band in the case of the cobalt-containing materials. We conclude there is no significant evidence for any significant local orthorhombic distortion in the materials.

All of the experimental data presented so far indicate that the substituent metals are randomly but homogeneously distributed
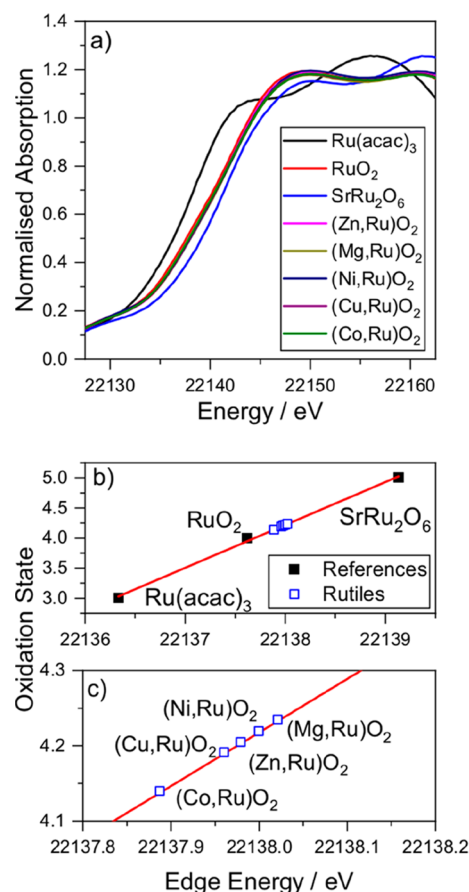


**Figure 3.** (a) Normalized Ru K-edge XANES spectra of substituted ruthenium oxides and reference compounds of known oxidation state ($Ru^{III}(acac)_3$, $Ru^{IV}O_2$, and $SrRu^{V}_2O_6$). (b) Plots of edge position as a function of oxidation state with linear fit of reference materials. (c) An expanded region of part b, showing the oxidation states of Ru in the substituted rutiles.

throughout the rutile structure, unlike materials with a similar composition produced by Krtil and co-workers.[21−25,41] In those materials, the substituents (Co, Ni, Zn, and Mg) were found to form localized clusters/layers, while maintaining lattice parameters virtually identical to those of $RuO_2$ and a constant oxidation state of ruthenium of 4+. In contrast, our new materials have expanded unit cell volumes when compared to $RuO_2$, which is to be expected when incorporating a cation with a larger ionic radius into the lattice, the absence of oxygen non-stoichiometry, and clear evidence for partial oxidation of Ru to balance charge. Although we cannot rule out any local clustering of the substituent cations in our materials, if this is present, it is likely to be only on a short length scale. Interestingly, upon heating the materials in air, they all show collapse and phase separation at temperatures above ~600 °C (Supporting Information): this suggests that they would be difficult to access by synthesis methods that involved annealing in air.

The magnetic response of the new materials also provides evidence for the homogeneity of the elemental substitution and shows an evolution of behavior when the diamagnetic substituents Mg and Zn are present (Figures 6a−c) that cannot be explained by phase-separated regions of $RuO_2$ and MO. For $RuO_2$, the increasing susceptibility at high temperature (>200 K) agrees with the recent report of itinerant antiferromagnetism in the material that persists to at least 300 K. The magnitude of the susceptibility of $RuO_2$ at 300 K ($2.5 \times 10^{-4}$ emu/mol of Ru) is
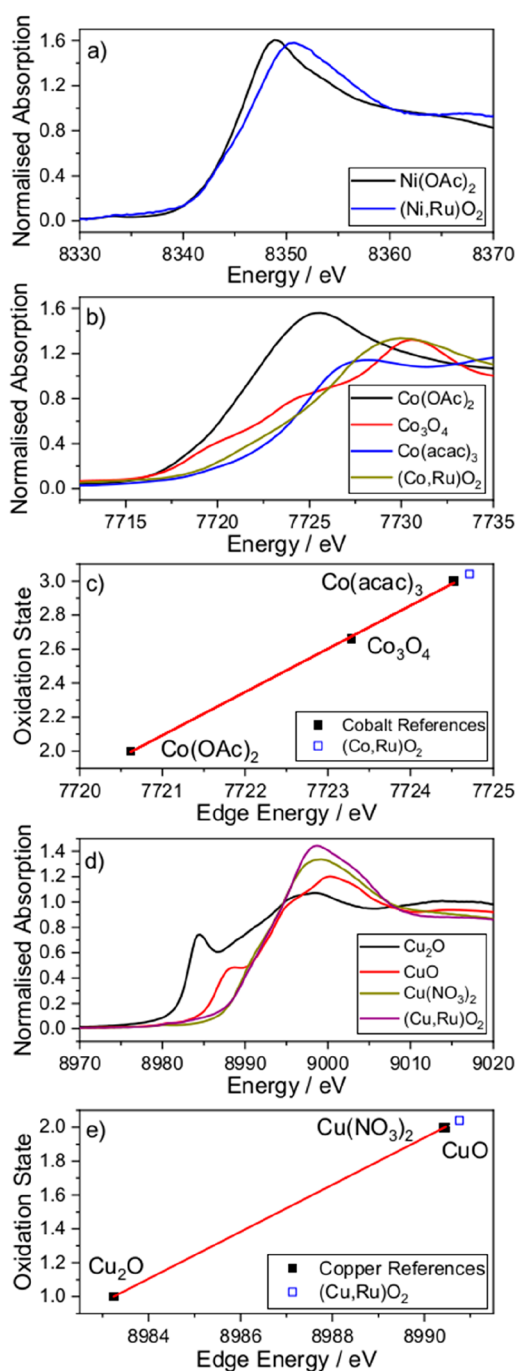
**Figure 4.** Normalized (a) Ni K-edge, (b) Co K-edge, and (d) Cu K-edge XANES spectra of substituted ruthenium oxides and reference compounds. Plots of (c) Co K-edge and (e) Cu K-edge position as a function of oxidation state with linear fit of reference materials.



**Figure 5.** Raman spectra of (a) $RuO_2$ and (b) zinc-, (c) magnesium-, (d) nickel-, (e) cobalt-, and (f) copper-substituted ruthenium oxides. The fitted functions to the spectra are represented by the colored shading: $E_{1g}$ in blue, $A_{1g}$ in pink, and $B_{2g}$ in brown.

only slightly larger than that reported by Berlijn et al.[5] This behavior is modified by inclusion of the substituent metals and instead the magnetic susceptibility, $\chi(T)$, increases with decreasing temperature for the field-cooled cooling curves over the entire temperature range investigated, implying a disruption of the ordering of the ruthenium moments. Furthermore, the susceptibility per ruthenium gradually increases with substitution of the diamagnetic Zn and Mg, consistent with the (partial) oxidation of the ruthenium to charge balance and a breakdown of the long-range antiferromagnetic order. The increase in
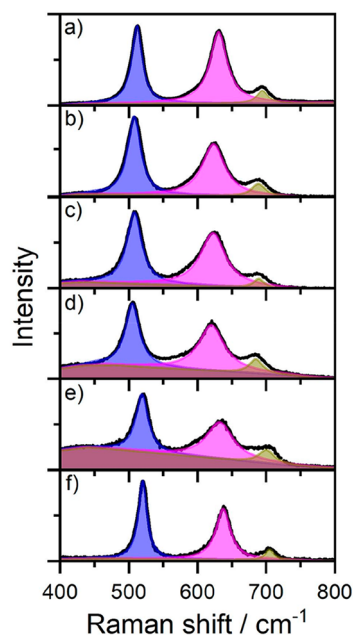
susceptibility is more pronounced for the paramagnetic substituents ($Cu^{2+}$, $Co^{3+}$, and $Ni^{2+}$) reaching $1 \times 10^{-3}$ emu/mol of Ru at 300 K for Co, Figure 6d−f. None of the samples exhibits a well-defined Curie−Weiss behavior, so extracting reliable values for either an effective moment or a Weiss temperature is not possible. Nevertheless, the magnitudes of the susceptibility at 300 K for the metal-substituted materials are consistent with the values expected for homogeneously distributed moments on paramagnetic $Cu^{2+}$, $Co^{3+}$, and $Ni^{2+}$ ions and a small moment, cf. $RuO_2$, on the Ru sites.

The temperature dependence of the susceptibility is reversible for pure $RuO_2$ with no difference between zero-field-cooled warming (ZFCW) and field-cooled cooling (FCC) curves, as expected for a system in an antiferromagnetically ordered state. The temperature dependence of the magnetic response of the other materials, and especially those that contain paramagnetic substituents ($Ni^{2+}$, $Cu^{2+}$, $Co^{3+}$), is more complex, Figure 6b−e. For the Zn-, Mg-, and Cu-substituted materials, differences between the ZFCW and FCC curves appear below ∼100 K. Some of this difference may be attributed to a small amount of condensed dioxygen contamination in the materials but also indicates that the antiferromagnetic Ru−Ru order in the pure $RuO_2$ is disrupted. For the Co- and Ni-substituted materials, a clear hysteresis at ∼25 K suggests a magnetic spin freezing. Further work would be required to establish the nature of these spin frozen states.

Figure 7 shows the electrocatalytic activity for all of the ruthenium oxides studied normalized to both mass of ruthenium and BET surface area. The parameters extracted from these measurements are shown in Table 4. The two $RuO_2$ samples provide benchmarks for extremes of activity and stability. Although there are many studies of $RuO_2$ already reported, it is rare to find comparable materials that have been studied under the same electrochemical conditions, especially as we have used more concentrated $H_2SO_4$ as electrolyte compared to most previous reports and have performed the tests at 60 °C rather

**Table 3. Fitted Parameters for $E_g$ and $A_{1g}$ Bands (Voigt Peak Shape Function) in the Raman Spectra of $RuO_2$ and Substituted Rutile Materials**

| material | $E_g$/cm$^{-1}$ | $E_g$ fwhm/ cm$^{-1}$ | $A_{1g}$/cm$^{-1}$ | $A_{1g}$ fwhm/ cm$^{-1}$ | $E_g/A_{1g}$ fwhm ratio |
|---|---|---|---|---|---|
| $RuO_2$ | 512.9(1) | 20.2(2) | 631.5(1) | 32.4(3) | 0.62(1) |
| $(Zn,Ru)O_2$ | 507.6(1) | 27(3) | 623.5(2) | 45.3(7) | 0.60(7) |
| $(Mg,Ru)O_2$ | 508.2(2) | 32.6(6) | 622.7(3) | 49(1) | 0.67(2) |
| $(Ni,Ru)O_2$ | 504.8(2) | 37(2) | 621.2(4) | 53(1) | 0.70(4) |
| $(Cu,Ru)O_2$ | 520.1(1) | 16.6(2) | 637.3(1) | 26.7(5) | 0.62(1) |
| $(Co,Ru)O_2$ | 519.1(1) | 24.5(5) | 631.7(3) | 54(1) | 0.45(1) |

than at room temperature. $RuO_2(A)$ is a highly crystalline $RuO_2$ (surface area 14.6 m$^2$ g$^{-1}$) and has relatively low mass activity and low Ru dissolution under the scanning conditions implemented here. On the other hand, $RuO_2(B)$, which has a surface area comparable to the substituted materials (37.5 m$^2$ g$^{-1}$) shows orders of magnitude higher activity but also much higher Ru dissolution. The activity of the substituted $(M_{1-x}Ru_x)O_2$ materials lies between the bounds of the two $RuO_2$ samples, with all being more active than the highly crystalline reference but somewhat less active than reference $RuO_2(B)$. The mass activities of the Cu, Ni, and Zn ruthenates are all essentially identical, with the Co- and Mg-substituted materials showing successively higher activities. When normalized for surface area, the Mg-substituted material remains the most active of the new solids.

The data in Table 4 highlight the leaching of the constituent metals from the oxides during electrocatalysis in the wet cell tests. The highly crystalline $RuO_2(A)$ shows little loss of Ru into solution, consistent with its low surface area, but in contrast, the high surface area $RuO_2(B)$ shows significant Ru loss, an order of magnitude higher than any of the substituted materials. This is expected for $RuO_2$ on application of electrochemical potential at acidic pH, and this is well-known from many previous studies.[42] The substituted $(M_{1-x}Ru_x)O_2$ materials, which have a comparable surface area, show a much lower level of Ru loss into solution but instead show a significant loss of the base metal. This occurs to the greatest extent for Co, followed by Mg, and then Cu, Zn, and Ni, which all show similar losses of the substituent metals. Interestingly, this mirrors the activity data already discussed, which may imply that the loss of the base metal creates an active form of Ru-rich oxide, or at least a surface enriched in Ru. This is a noteworthy observation, since the electrochemical activity of a number of ruthenium and iridium oxides has recently been linked to the leaching of base metal ions into solution to yield the catalytically active material, such as in $Y_2Ir_2O_7$,[43] $A_2Ru_2O_7$ (A = Yb, Gd, Nd),[44] and $SrRuO_3$.[45,46] Of the materials that we have studied, $Co_xRu_{1-x}O_2$ is the only one that shows an increase in activity at end of life, which is probably due to its increase in surface area, as seen from the change in capacitance (Supporting Information) from beginning to end of life.

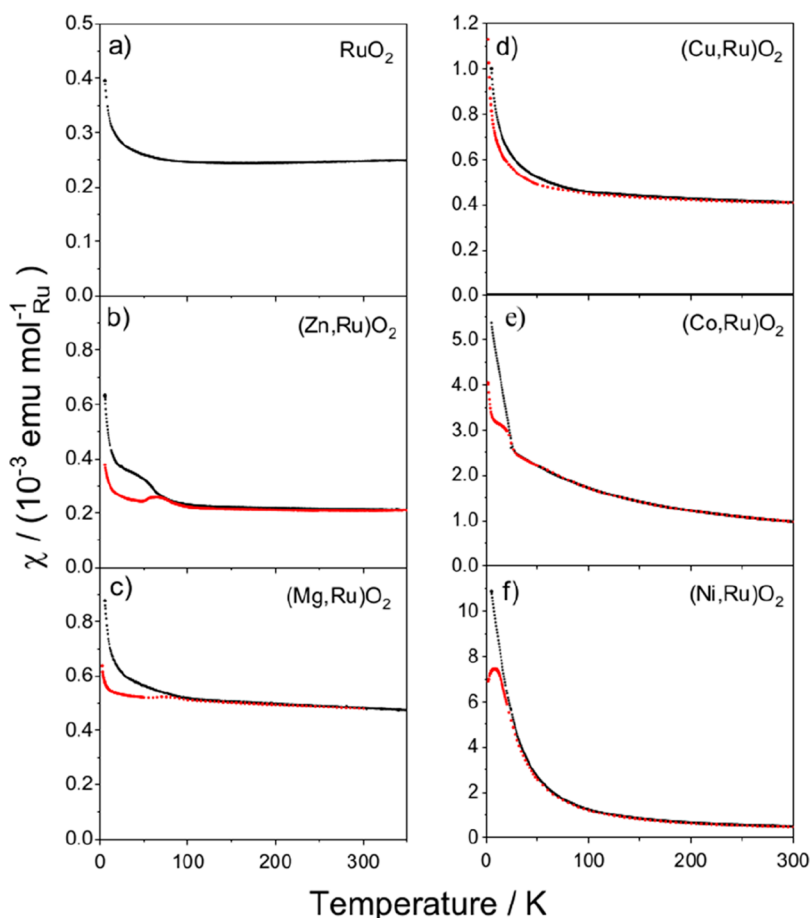Tafel plots taken between 1.4 and 1.45 V vs RHE, Figure 8, show similar gradients (between 40 and 50 mV dec$^{-1}$) and



**Figure 6.** Magnetic susceptibility as a function of temperature in an applied field of 1 kOe for (a) $RuO_2$ and (b) zinc-, (c) magnesium-, (d) copper-, (e) cobalt-, and (f) nickel-substituted ruthenium oxides. Zero-field-cooled warming (red symbols) and field-cooled cooling (black symbols) data are shown for the metal-substituted samples.
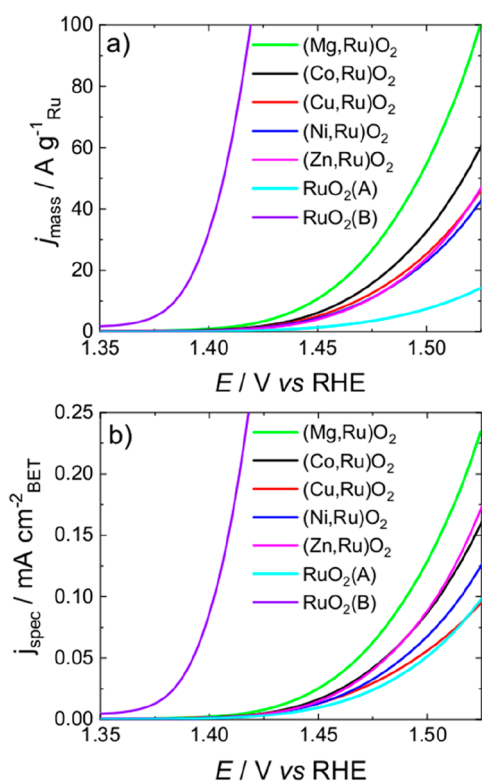
**Figure 7.** Electrocatalytic activity of the ruthenium oxides normalized by (a) mass of Ru and (b) BET surface area.



**Figure 8.** Tafel plots of the ruthenium oxides; see Table 4 for the gradients extracted.

thus suggest that all catalysts operate through the same reaction mechanism. The values of Tafel slope reported in the literature for $RuO_2$ can vary significantly between different samples, being dependent on the surface area and crystallinity of the materials; for example, Iwakura et al. showed that the value measured for films of $RuO_2$ increased from 40 to 70 mV dec$^{-1}$ with an increase in annealing temperature of the electrocatalyst.[47] Typically, however, a value of ~40 mV dec$^{-1}$ is found for many $RuO_2$ samples reported in the literature.[48] The value of the Tafel slope has been used to infer mechanistic information about the OER process in oxides: at 25 °C, values of ~120 mV dec$^{-1}$ have been interpreted as arising the case when the first electron transfer step in a sequential reaction is rate-d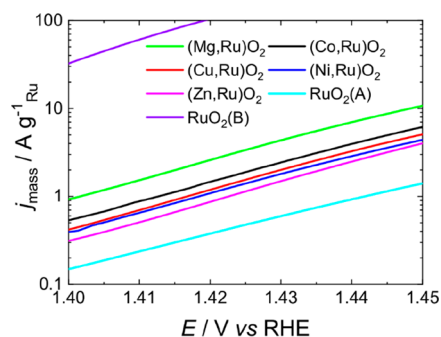etermining, values of ~40 mV dec$^{-1}$ if a second electron transfer step is rate-determining, and intermediate values of ~60 mV dec$^{-1}$ when the rate-determining step involves a chemical step subsequent to the first electron transfer.[48] Note that at 60 °C, as in the experiments here, this gradient is expected to be higher, so that a second electron transfer step as rate-determining would give a Tafel slope of ~45 mV dec$^{-1}$, in line with our observations.

Table 4 also contains the results from activity toward OER in a membrane electrode assembly (MEA), as would be used in an electrolyzer. In the MEA test, we have compared with a mixed ruthenium−iridium oxide, which is commonly used in such situations: it is clear that the new substituted materials show considerably higher activities than this reference material and lower onset voltages for OER. It is important to note that the correlation of activity in the MEA with the wet cell activities is not always obvious. For example, $Mg_xRu_{1−x}O_x$ has the lowest activity in MEA testing at beginning of life among the substituted rutiles, despite having the highest activity in the wet cell tests, but then maintains its activity better than Zn, Ni, and Cu. The reason for the difference between wet cell and MEA results is most likely to be due to the leaching of the metal ions: during the preparation of the MEA, the processing with the highly acidic Nafion ionomer binder provides a different medium in which the extraction of metal ions may occur, and their presence in the ionomer may then inhibit the activity of the MEA, as seen previously in work on fuel cells.[49,50] This implies that the wet cell testing data cannot be used as a measure, or screening protocol, of likely OER activity in an MEA.

## ■ CONCLUSIONS

A low temperature hydrothermal synthesis of a series of substituted ruthenium oxide rutiles allows access to homogeneous

## Table 4. Results of Electrocatalytic Testing of the Ruthenium Oxides

| | | wet cell testing | | | | | MEA testing | | | |
| | | mass activity/A g$^{-1}$$_{PGM}$ at 1.5 V vs RHE | | % dissolution | | | mass activity/A g$^{-1}$$_{PGM}$ at 1.5 V | | OER onset voltage[a]/V | |
| material | BET surface area/ m$^2$ g$^{-1}$ | beginning of life | end of life | loss of M | loss of Ru | Tafel slope/ mV dec$^{-1}$ | beginning of life | end of life | beginning of life | end of life |
|---|---|---|---|---|---|---|---|---|---|---|
| $(Zn,Ru)O_2$ | 27.1 | 34 | 28 | 10.5 | 0.02 | 44.0 | 3093 | 2680 | 1.399 | 1.416 |
| $(Mg,Ru)O_2$ | 42.5 | 83 | 63 | 35.4 | 0.28 | 44.4 | 2634 | 2291 | 1.395 | 1.413 |
| $(Ni,Ru)O_2$ | 33.9 | 31 | 30 | 7.8 | 0.11 | 45.5 | 3052 | 1556 | 1.385 | 1.399 |
| $(Co,Ru)O_2$ | 37.6 | 55 | 69 | 91.4 | 0.37 | 45.0 | 3447 | 3839 | 1.4 | 1.397 |
| $(Cu,Ru)O_2$ | 45.8 | 34 | 32 | 10.6 | 0.34 | 45.4 | 2812 | 1497 | 1.383 | 1.412 |
| $RuO_2$(A) | 14.6 | 10 | 7 | n/a | <0.02 | 50.0 | | | | |
| $RuO_2$(B) | 37.5 | 1015[b] | 903 | n/a | 7.8 | 39.5 | | | | |
| $(Ir,Ru)O_x$ | 8.0 | 10 | | 0.065[c] | 0.013[c] | 46.0 | 334 | 302 | 1.458 | 1.461 |

[a]1 mA cm$^{-2}$$_{Geo}$ above the background current (measured at 1.23 V vs RHE, typically between 2.3 and 3.9 mA cm$^{-2}$$_{Geo}$). [b]Extrapolated data, last data point 660 A g$^{-1}$ at 1.475 V. [c]1500 cycles at 0.6−1.35 V vs RHE at 100 mV s$^{-1}$.

materials by direct crystallization from solution. These ternary materials decompose into their substituent oxides upon heating in air, suggesting it would be challenging to synthesize them at elevated temperatures in the solid state, or indeed via a coprecipitation approach where firing is needed to bring about crystallinity. By using XANES spectroscopy and neutron diffraction, we have shown how the divalent substituent metals have been incorporated into the structure through partial oxidation of the ruthenium, which is corroborated by magnetization measurements. The materials show favorable activity for oxygen evolution in acid electrolytes, compared to some benchmark reference samples. Significantly, the addition of a partner metal lowers the activity compared to a high surface area $RuO_2$ but results in a much lower dissolution of Ru into solution with instead the partner metal being leached. The leaching of the partner metals in ternary ruthenates has recently been observed in other structural families that have been proposed as highly active electrocatalysts and is clearly an important consideration when designing new acid-resilient electrocatalysts. We propose here that this dissolution of cations means that there is not necessarily any correlation between electrocatalytic activity in wet-cell electrochemistry data and in membrane electrode assemblies: the loss of metal ions during electrocatalysis may affect the operation of the MEA depending on the conditions of its preparation.

## ASSOCIATED CONTENT

### Ⓢ Supporting Information

The Supporting Information is available free of charge at https://pubs.acs.org/doi/10.1021/acs.chemmater.0c01884.

> Characterization data for peroxide precursors and thermodiffraction, thermogravimetric, and electrochemical data from rutile materials (PDF)

## AUTHOR INFORMATION

### Corresponding Author

**Richard I. Walton** − *Department of Chemistry, University of Warwick, Coventry CV4 7AL, U.K.;* ⓞ orcid.org/0000-0001-9706-2774; Email: r.i.walton@warwick.ac.uk

### Authors

**David L. Burnett** − *Department of Chemistry, University of Warwick, Coventry CV4 7AL, U.K.*

**Enrico Petrucco** − *Johnson Matthey Technology Centre, Reading RG4 9NH, U.K.*

**Katie M. Rigg** − *Johnson Matthey Technology Centre, Reading RG4 9NH, U.K.*

**Christopher M. Zalitis** − *Johnson Matthey Technology Centre, Reading RG4 9NH, U.K.;* ⓞ orcid.org/0000-0001-9139-2254

**Jamie G. Lok** − *Department of Chemistry, University of Warwick, Coventry CV4 7AL, U.K.*

**Reza J. Kashtiban** − *Department of Physics, University of Warwick, Coventry CV4 7AL, U.K.*

**Martin R. Lees** − *Department of Physics, University of Warwick, Coventry CV4 7AL, U.K.*

**Jonathan D. B. Sharman** − *Johnson Matthey Technology Centre, Reading RG4 9NH, U.K.*

Complete contact information is available at:
https://pubs.acs.org/10.1021/acs.chemmater.0c01884

## REFERENCES

(1) Ryden, W. D.; Lawson, A. W. Magnetic Susceptibility of $IrO_2$ and $RuO_2$. *J. Chem. Phys.* **1970**, *52*, 6058−6061.

(2) Kodintsev, I. M.; Trasatti, S. Electrocatalysis of $H_2$ evolution on $RuO_2$ + $IrO_2$ mixed oxide electrodes. *Electrochim. Acta* **1994**, *39*, 1803−1808.

(3) Murphy, D. W.; Disalvo, F. J.; Carides, J. N.; Waszczak, J. V. Topochemical reactions of rutile related structures with lithium. *Mater. Res. Bull.* **1978**, *13*, 1395−1402.

(4) Witczak-Krempa, W.; Chen, G.; Kim, Y. B.; Balents, L. Correlated Quantum Phenomena in the Strong Spin-Orbit Regime. *Annu. Rev. Condens. Matter Phys.* **2014**, *5*, 57−82.

(5) Berlijn, T.; Snijders, P. C.; Delaire, O.; Zhou, H. D.; Maier, T. A.; Cao, H. B.; Chi, S. X.; Matsuda, M.; Wang, Y.; Koehler, M. R.; Kent, P. R. C.; Weitering, H. H. Itinerant Antiferromagnetism in $RuO_2$. *Phys. Rev. Lett.* **2017**, *118*, No. 077201.

(6) Rossmeisl, J.; Qu, Z. W.; Zhu, H.; Kroes, G. J.; Norskov, J. K. Electrolysis of water on oxide surfaces. *J. Electroanal. Chem.* **2007**, *607*, 83−89.

(7) Lee, Y.; Suntivich, J.; May, K. J.; Perry, E. E.; Shao-Horn, Y. Synthesis and Activities of Rutile $IrO_2$ and $RuO_2$ Nanoparticles for Oxygen Evolution in Acid and Alkaline Solutions. *J. Phys. Chem. Lett.* **2012**, *3*, 399−404.

(8) Yu, J.; He, Q. J.; Yang, G. M.; Zhou, W.; Shao, Z. P.; Ni, M. Recent Advances and Prospective in Ruthenium-Based Materials for Electrochemical Water Splitting. *ACS Catal.* **2019**, *9*, 9973−10011.

(9) Tunold, R.; Marshall, A. T.; Rasten, E.; Tsypkin, M.; Owe, L. E.; Sunde, S. Materials for Electrocatalysis of Oxygen Evolution Process in PEM Water Electrolysis Cells. In *Electrochemistry: Symposium on Interfacial Electrochemistry in Honor of Brian E. Conway*; MacDougall, B. R., Gileadi, E., Leddy, J., Trasatti, S., Bock, C., Gottesfeld, S., Scrosati, B., Morin, S., Eds.; Electrochemical Soc Inc: Pennington, NJ, 2010; Vol. 25, pp 103−117.

(10) Reier, T.; Nong, H. N.; Teschner, D.; Schlogl, R.; Strasser, P. Electrocatalytic Oxygen Evolution Reaction in Acidic Environments - Reaction Mechanisms and Catalysts. *Adv. Energy Mater.* **2017**, *7*, No. 1601275.

(11) Balaya, P.; Li, H.; Kienle, L.; Maier, J. Fully reversible homogeneous and heterogeneous Li storage in $RuO_2$ with high capacity. *Adv. Funct. Mater.* **2003**, *13*, 621−625.

(12) Hassan, A. S.; Moyer, K.; Ramachandran, B. R.; Wick, C. D. Comparison of Storage Mechanisms in $RuO_2$, $SnO_2$, and $SnS_2$ for Lithium-Ion Battery Anode Materials. *J. Phys. Chem. C* **2016**, *120*, 2036−2046.

(13) Hu, Y. Y.; Liu, Z. G.; Nam, K. W.; Borkiewicz, O. J.; Cheng, J.; Hua, X.; Dunstan, M. T.; Yu, X. Q.; Wiaderek, K. M.; Du, L. S.; Chapman, K. W.; Chupas, P. J.; Yang, X. Q.; Grey, C. P. Origin of

additional capacities in metal oxide lithium-ion battery electrodes. *Nat. Mater.* **2013**, *12*, 1130−1136.

(14) Kötz, R.; Stucki, S. Stabilization of $RuO_2$ by $IrO_2$ for anodic oxygen evolution in acid media. *Electrochim. Acta* **1986**, *31*, 1311−1316.

(15) Owe, L. E.; Tsypkin, M.; Wallwork, K. S.; Haverkamp, R. G.; Sunde, S. Iridium-ruthenium single phase mixed oxides for oxygen evolution: Composition dependence of electrocatalytic activity. *Electrochim. Acta* **2012**, *70*, 158−164.

(16) Kasian, O.; Geiger, S.; Stock, P.; Polymeros, G.; Breitbach, B.; Savan, A.; Ludwig, A.; Cherevko, S.; Mayrhofer, K. J. J. On the Origin of the Improved Ruthenium Stability in $RuO_2$-$IrO_2$ Mixed Oxides. *J. Electrochem. Soc.* **2016**, *163*, F3099−F3104.

(17) Onuchukwu, A. I.; Trasatti, S. Effect of substitution of $SnO_2$ for $TiO_2$ on the surface and electrocatalytic properties of $RuO_2$+$TiO_2$ electrodes. *J. Appl. Electrochem.* **1991**, *21*, 858−862.

(18) Wu, X.; Tayal, J.; Basu, S.; Scott, K. Nano-crystalline $Ru_xSn_{1-x}O_2$ powder catalysts for oxygen evolution reaction in proton exchange membrane water electrolysers. *Int. J. Hydrogen Energy* **2011**, *36*, 14796−14804.

(19) Tilak, B. V.; Tari, K.; Hoover, C. L. Metal Anodes and Hydrogen Cathodes: Their Activity Towards $O_2$ Evolution and $ClO_3^-$ Reduction Reactions. *J. Electrochem. Soc.* **1988**, *135*, 1386−1392.

(20) Lin, Y. C.; Tian, Z. Q.; Zhang, L. J.; Ma, J. Y.; Jiang, Z.; Deibert, B. J.; Ge, R. X.; Chen, L. Chromium-ruthenium oxide solid solution electrocatalyst for highly efficient oxygen evolution reaction in acidic media. *Nat. Commun.* **2019**, *10*, No. 162.

(21) Petrykin, V.; Macounova, K.; Shlyakhtin, O. A.; Krtil, P. Tailoring the Selectivity for Electrocatalytic Oxygen Evolution on Ruthenium Oxides by Zinc Substitution. *Angew. Chem., Int. Ed.* **2010**, *49*, 4813−4815.

(22) Petrykin, V.; Macounova, K.; Franc, J.; Shlyakhtin, O.; Klementova, M.; Mukerjee, S.; Krtil, P. Zn-Doped $RuO_2$ electrocatalysts for Selective Oxygen Evolution: Relationship between Local Structure and Electrocatalytic Behavior in Chloride Containing Media. *Chem. Mater.* **2011**, *23*, 200−207.

(23) Petrykin, V.; Bastl, Z.; Franc, J.; Macounova, K.; Makarova, M.; Mukerjee, S.; Ramaswamy, N.; Spirovova, I.; Krtil, P. Local Structure of Nanocrystalline $Ru_{1-x}Ni_xO_{2-\delta}$ Dioxide and Its Implications for Electrocatalytic Behavior—An XPS and XAS Study. *J. Phys. Chem. C* **2009**, *113*, 21657−21666.

(24) Abbott, D. F.; Petrykin, V.; Okube, M.; Bastl, Z.; Mukerjee, S.; Krtil, P. Selective Chlorine Evolution Catalysts Based on Mg-Doped Nanoparticulate Ruthenium Dioxide. *J. Electrochem. Soc.* **2015**, *162*, H23−H31.

(25) Petrykin, V.; Macounova, K.; Okube, M.; Mukerjee, S.; Krtil, P. Local structure of Co doped $RuO_2$ nanocrystalline electrocatalytic materials for chlorine and oxygen evolution. *Catal. Today* **2013**, *202*, 63−69.

(26) Hiley, C. I.; Lees, M. R.; Fisher, J. M.; Thompsett, D.; Agrestini, S.; Smith, R. I.; Walton, R. I. Ruthenium(V) Oxides from Low-Temperature Hydrothermal Synthesis. *Angew. Chem., Int. Ed.* **2014**, *53*, 4423−4427.

(27) Hiley, C. I.; Scanlon, D. O.; Sokol, A. A.; Woodley, S. M.; Ganose, A. M.; Sangiao, S.; De Teresa, J. M.; Manuel, P.; Khalyavin, D. D.; Walker, M.; Lees, M. R.; Walton, R. I. Antiferromagnetism at T > 500 K in the layered hexagonal ruthenate $SrRu_2O_6$. *Phys. Rev. B: Condens. Matter Mater. Phys.* **2015**, *92*, 104413.

(28) Hiley, C. I.; Lees, M. R.; Hammond, D. L.; Kashtiban, R. J.; Sloan, J.; Smith, R. I.; Walton, R. I. $Ba_4Ru_3O_{10.2}(OH)_{1.8}$: a new member of the layered hexagonal perovskite family crystallised from water. *Chem. Commun.* **2016**, *52*, 6375−6378.

(29) Hiley, C. I.; Walton, R. I. Controlling the crystallisation of oxide materials by solvothermal chemistry: tuning composition, substitution and morphology of functional solids. *CrystEngComm* **2016**, *18*, 7656−7670.

(30) Prasad, B. E.; Kazin, P.; Komarek, A. C.; Felser, C.; Jansen, M. beta-$Ag_3RuO_4$, a Ruthenate(V) Featuring Spin Tetramers on a Two-Dimensional Trigonal Lattice. *Angew. Chem., Int. Ed.* **2016**, *55*, 4467−4471.

(31) Prasad, B. E.; Kanungo, S.; Jansen, M.; Komarek, A. C.; Yan, B. H.; Manuel, P.; Felser, C. $AgRuO_3$, a Strongly Exchange-Coupled Honeycomb Compound Lacking Long-Range Magnetic Order. *Chem. - Eur. J.* **2017**, *23*, 4680−4686.

(32) Pankratov, D. A.; Portachenko, T. A.; Perfiliev, Y. D. Emission moessbauer studies of the "cobalt peroxide". *Moscow Univ. Chem. Bull.* **2008**, *49*, 349−353.

(33) Williams, W. G.; Ibberson, R. M.; Day, P.; Enderby, J. E. GEM - General Materials Diffractometer at ISIS. *Phys. B* **1997**, *241−243*, 234−236.

(34) Larson, A. C.; Dreele, R. B. V. Los Alamos National Laboratory Report LAUR 86-748; 2000.

(35) Dent, A. J.; Cibin, G.; Ramos, S.; Smith, A. D.; Scott, S. M.; Varandas, L.; Pearson, M. R.; Krumpa, N. A.; Jones, C. P.; Robbins, P. E. B18: A core XAS spectroscopy beamline for Diamond. *J. Phys. Conf. Ser.* **2009**, *190*, No. 012039.

(36) Ravel, B.; Newville, M. ATHENA, ARTEMIS, HEPHAESTUS: data analysis for X-ray absorption spectroscopy using IFEFFIT. *J. Synchrotron Radiat.* **2005**, *12*, 537−541.

(37) Bolzan, A. A.; Fong, C.; Kennedy, B. J.; Howard, C. J. Structural studies of rutile-type metal dioxides. *Acta Crystallogr., Sect. B: Struct. Sci.* **1997**, *53*, 373−380.

(38) Abrahams, I.; Bruce, P. G.; David, W. I. F.; West, A. R. Structure determination of substituted rutiles by time-of-flight neutron diffraction. *Chem. Mater.* **1989**, *1*, 237−240.

(39) Huang, Y. S.; Pollak, F. H. Raman investigation of rutile $RuO_2$. *Solid State Commun.* **1982**, *43*, 921−924.

(40) Rosenblum, S. S.; Weber, W. H.; Chamberland, B. L. Raman-scattering observation of the rutile-to-$CaCl_2$ phase transition in $RuO_2$. *Phys. Rev. B: Condens. Matter Mater. Phys.* **1997**, *56*, 529−533.

(41) Abbott, D. F.; Mukerjee, S.; Petrykin, V.; Bastl, Z.; Halck, N. B.; Rossmeisl, J.; Krtil, P. Oxygen reduction on nanocrystalline ruthenia - local structure effects. *RSC Adv.* **2015**, *5*, 1235−1243.

(42) Roy, C.; Rao, R. R.; Stoerzinger, K. A.; Hwang, J.; Rossmeisl, J.; Chorkendorff, I.; Shao-Horn, Y.; Stephens, I. E. L. Trends in Activity and Dissolution on $RuO_2$ under Oxygen Evolution Conditions: Particles versus Well-Defined Extended Surfaces. *ACS Energy Lett.* **2018**, *3*, 2045−2051.

(43) Lebedev, D.; Povia, M.; Waltar, K.; Abdala, P. M.; Castelli, I. E.; Fabbri, E.; Blanco, M. V.; Fedorov, A.; Coperet, C.; Marzari, N.; Schmidt, T. J. Highly Active and Stable Iridium Pyrochlores for Oxygen Evolution Reaction. *Chem. Mater.* **2017**, *29*, 5182−5191.

(44) Abbott, D. F.; Pittkowski, R. K.; Macounova, K.; Nebel, R.; Marelli, E.; Fabbri, E.; Castelli, I. E.; Krtil, P.; Schmidt, T. J. Design and Synthesis of Ir/Ru Pyrochlore Catalysts for the Oxygen Evolution Reaction Based on Their Bulk Thermodynamic Properties. *ACS Appl. Mater. Interfaces* **2019**, *11*, 37748−37760.

(45) Chang, S. H.; Danilovic, N.; Chang, K. C.; Subbaraman, R.; Paulikas, A. P.; Fong, D. D.; Highland, M. J.; Baldo, P. M.; Stamenkovic, V. R.; Freeland, J. W.; Eastman, J. A.; Markovic, N. M. Functional links between stability and reactivity of strontium ruthenate single crystals during oxygen evolution. *Nat. Commun.* **2014**, *5*, No. 4191.

(46) Kim, B. J.; Abbott, D. F.; Cheng, X.; Fabbri, E.; Nachtegaal, M.; Bozza, F.; Castelli, I. E.; Lebedev, D.; Schaublin, R.; Coperet, C.; Graule, T.; Marzari, N.; Schmidt, T. J. Unraveling Thermodynamics, Stability, and Oxygen Evolution Activity of Strontium Ruthenium Perovskite Oxide. *ACS Catal.* **2017**, *7*, 3245−3256.

(47) Iwakura, C.; Hirao, K.; Tamura, H. Preparation of ruthenium dioxide electrodes and their anodic polarization characteristics in acidic solutions. *Electrochim. Acta* **1977**, *22*, 335−340.

(48) Doyle, R. L.; Godwin, I. J.; Brandon, M. P.; Lyons, M. E. G. Redox and electrochemical water splitting catalytic properties of hydrated metal oxide modified electrodes. *Phys. Chem. Chem. Phys.* **2013**, *15*, 13737−13783.

(49) Antolini, E.; Salgado, J. R. C.; Gonzalez, E. R. The stability of Pt-M (M = first row transition metal) alloy catalysts and its effect on

the activity in low temperature fuel cells - A literature review and tests on a Pt-Co catalyst. *J. Power Sources* **2006**, *160*, 957−968.

(50) Ahluwalia, R. K.; Wang, X.; Peng, J. K.; Kariuki, N. N.; Myers, D. J.; Rasouli, S.; Ferreira, P. J.; Yang, Z.; Martinez-Bonastre, A.; Fongalland, D.; Sharman, J. Durability of De-Alloyed Platinum-Nickel Cathode Catalyst in Low Platinum Loading Membrane-Electrode Assemblies Subjected to Accelerated Stress Tests. *J. Electrochem. Soc.* **2018**, *165*, F3316−F3327.

(51) Walton, R. I.; Burnett, D. L.; Playford, H. Y.; Tucker, M. G.; 2015, Structures of New Doped $RuO_2$ Rutiles, STFC ISIS Neutron and Muon Source, https://doi.org/10.5286/ISIS.E.RB1510110